The importance of modelling ballast particle shape in the discrete element method

M. Lu · G. R. McDowell

Abstract The discrete element method has been used to model railway ballast. Particles have been modelled using both spheres and clumps of spheres. A simple procedure has been developed to generate clumps which resemble real ballast particles much more so than spheres. The influence of clump shape on the heterogeneous stresses within an aggregate has been investigated, and it has been found that more angular clumps lead to a greater degree of homogeneity. A box test consisting of one cycle of sleeper load after compaction has been performed on an aggregate of spheres and also on an alternative aggregate of clumps. The interlocking provided by the clumps provides a much more realistic load-deformation response than the spheres and the clumps will be the basis for future work on ballast degradation under cyclic loading.

Keywords Discrete element modelling · Railway ballast · Particle geometry

1 Introduction

Since railway ballast in the track generally comprises large particles of typical size approximately 40 mm, it is difficult to treat such a material as a continuum, and the discrete element method (DEM) [1] offers a means of obtaining micro-mechanical insight into its behaviour. For this purpose the program PFC^{3D} [2] has been

M. Lu · G. R. McDowell (✉)
Nottingham Centre for Geomechanics,
School of Civil Engineering,
University of Nottingham,
Nottingham NG7 2RD, UK
e-mail: glenn.mcdowell@nottingham.ac.uk

used. PFC^{3D} is a discrete element program that has the ability to model entire boundary value problems directly with a large number of particles. The program contains two entities: a ball and a wall. Crushable particles can be simulated by forming agglomerates of bonded balls. Contact forces are used to calculate the accelerations of each ball using Newton's Second Law, and the accelerations are integrated to give velocities and displacements (and hence new contact forces via a contact constitutive law), via an explicit time-stepping scheme. Details can be found in the Itasca Manual [2], but for clarity key details will be provided later in the paper. The method has been used successfully to model single particle crushing tests for sand [3, 4] and one-dimensional compression tests on aggregates of sand [4, 5], and also triaxial tests [4, 6, 7]. Lim and McDowell [8] investigated the use of DEM for modelling railway ballast subjected to single particle crushing tests, oedometer tests and box tests involving cyclic loading on a simulated railway sleeper. They found that DEM was capable of simulating particle fracture and particle interlock. Particle fracture was achieved by bonding small balls together to form agglomerates of ballast size, whilst in the box tests clumps of overlapping balls were used to reduce computational time. A clump is a single entity of overlapping balls; internal overlapping contacts are ignored in calculations. In the box tests by Lim and McDowell [8], the clumps were simple cubic clumps of eight spheres, so the shape did not resemble that of a real ballast particle. This paper presents a simple procedure used to model ballast particle shape using many overlapping balls of different sizes to form complex clumps resembling real ballast particles. The parameters affecting the clump shape are described and examples of clumps using different parameters are presented. In addition, the distribution of contact forces is

examined in an aggregate of spheres and two alternative aggregates of clumps created using different parameters, in order to show the effect of the particle shape on the inhomogeneous stresses induced within the particle assembly. The result of the application of a cycle of load in a box test on clumps is compared with that for a box test on spheres.

2 Modelling ballast particle shape

2.1 General description

Figure 1 shows a typical real ballast particle. The aim is to begin to model such a complex shape using DEM. For this purpose, overlapping balls are used to form clumps using a simple procedure which gives control over the sphericity, angularity and surface texture of the clump.

A ball is created at the centre of a cubic cell to form the main body of the clump (although each clump remains fixed in position during the generation process, it can freely rotate in all directions during the box tests, decribed later in section 3). Fourteen directions are created: six orthogonal to the cube faces (i.e. in positive and negative directions along each orthogonal axis), and eight along the cube space diagonals, as shown in Fig. 2. All balls in the clump are created within a virtual sphere with a radius R_v. Along each direction, it is

possible to generate balls to form the clump; however, the directions of ball generation are chosen at random, and not all directions might be deployed. First, either only the 6 directions orthogonal to the cube faces are chosen for possible ball generation, or all 14 directions are chosen as possibilities. The likely number of directions used for ball generation is chosen as n and the probability p that a particular direction might be used is then $n/6$ if only the directions orthogonal to the cube spaces are used as possible directions, and $n/14$ if the space diagonals are also used. For each direction then, a random number r is drawn from uniform distribution in the range [0.0, 1.0]. If r is less than or equal to p, then this direction is chosen to generate balls. The number of balls generated in each direction is set directly. Figure 3 shows the ball generation process in one direction. The radius of the second ball formed is less than the radius of the first one. The difference in the radii of successively generated balls is a uniformly distributed random variable in the range $[0.0, c]$, where c is the maximum possible difference and is chosen directly. In this way, the angle subtended by the common tangents to successively generated spheres, is created at random, and the maximum angle is controlled partly by c (see below). Figure 4 shows the clump geometry and generation along a typical direction x. The centre of the second ball is derived from the centre of the first one and reduction in radius. The first ball with radius R_1 is centred at A(x_1, y_1, z_1) and the second ball with radius R_2 is centred at B(x_2, y_2, z_2). The angle 2α is the angle subtended by the two common tangents to the spheres. It can be seen that

$$x_2 = x_1 + D_1 \tag{1}$$
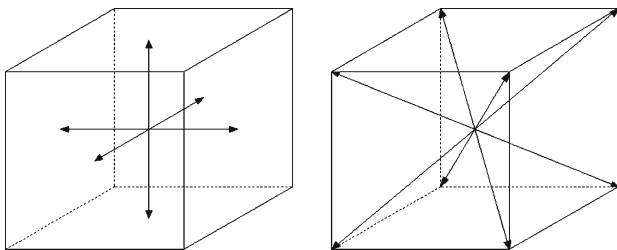$$y_2 = y_1 \tag{2}$$
$$z_2 = z_1 \tag{3}$$
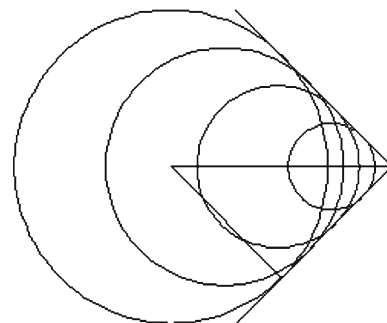$$R_1 = D_1 + D_2 \tag{4}$$
$$R_2 = D_2 + D_3 \tag{5}$$
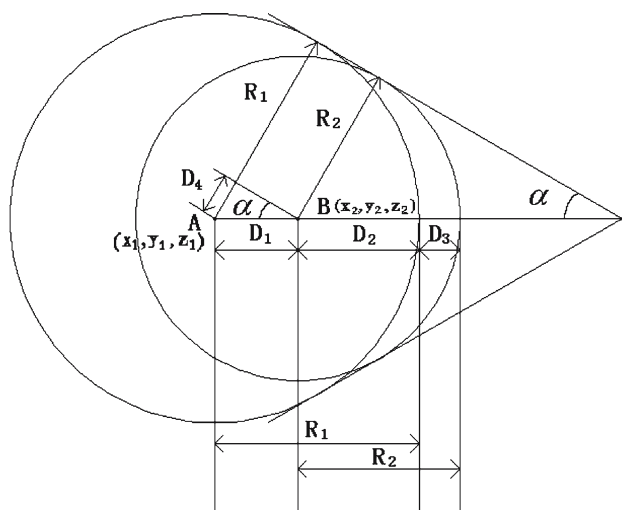$$R_1 - R_2 = D_4 \tag{6}$$

Fig. 1 Typical full-sized ballast particle

Fig. 2 Directions of ball generation for clumps

Fig. 3 Ball generation along one direction

Fig. 4 Definition of clump geometry

where D_4 is the reduction of radius in the range $[0.0, c]$.

Substituting Eqs. (4) and (5) into (6) yields

$$D_1 = D_3 + D_4. \tag{7}$$

Substituting (7) in (1):

$$x_2 = x_1 + D_3 + D_4 \tag{8}$$

where D_3 is the clump extension parameter and is constant and is chosen by the user.

The relationship between D_4, D_3 and α is given by

$$\sin \alpha = \frac{D_4}{D_3 + D_4} = \left(1 + \frac{D_3}{D_4}\right)^{-1} \tag{9}$$

The parameters D_3, c (and hence D_4), and the number of balls generated along each direction each have an influence on the sphericity of the particle. The ratio D_3/D_4 controls the angle α which will influence the sphericity depending on the number of balls used. Figure 5 shows the effect of using different values of α to generate clumps, shown for a constant value of D_3. In Fig. 5 the value of α and hence D_4 is constant for each generated ball and the maximum permissible number of balls have been shown; in the simulations described in section 2.2 below, the value of D_4 is a uniformly distributed random variable in the range $[0.0, c]$ and is chosen at random for each ball generated. A high sphericity would be achieved with a low value of D_3, a high value of D_4, and a small number of balls. The value of D_4 and the number of balls used also influence the angularity since this will determine the size of the smallest ball. Using a large number of balls with small extension D_3 can be used to produce flatter particle surfaces. After all the selected directions for ball generation have been used, balls are used to link up outermost balls of adjacent

directions in order to form edges of the clump. A line is used to join the outermost balls, and a series of balls inserted in between, as shown in Fig. 6. The radii of these balls vary linearly from one outermost ball to the other, and the number of such balls for each edge, set directly, affects the fineness or surface texture of the modelled ballast particle. The greater the number of balls used in each edge, the more 'realistic' the clump.

2.2 Results

Table 1 shows the parameters used for five different samples of clumps. Figure 7 shows some examples of the clumps formed using these parameters. It can be seen that realistic clumps can be formed by choosing a small extension between the clumps D_3 and large maximum value c in the reduction in ball size D_4, which is chosen at random for each generated ball; this tends to give large values of α and serves to produce simulated ballast which is reasonably equi-dimensional as is required by the Railtrack Line Specification for track ballast in the UK [9].

3 Box test simulations

3.1 General description

McDowell et. al. [10] describe box tests on ballast involving applied cyclic load to a simulated sleeper on ballast in a box of dimensions $700 \, \text{mm} \times 300 \, \text{mm} \times 450 \, \text{mm}$. The test set-up is shown in Fig. 8. Lim and McDowell [8] describe discrete element modelling of this ballast using a sphere to represent each ballast particle, and also using a simple eight-ball cubic clump. This work is extended here to using the new clumps developed in section 2, to examine the effect of clump shape on the distribution of contact forces and also the cyclic response of the aggregate in the box test.

3.2 Results

Figure 9 shows the simulated box test arrangements for the spheres, and for samples using two alternative clump shapes, described in Table 2. The box has dimensions $700 \, \text{mm} \times 300 \, \text{mm} \times 450 \, \text{mm}$. Figure 9a shows the box with 1,936 spheres, each of diameter 36.25 mm prior to loading. The sample was compacted by enhanced gravity and reducing gravity to $9.81 \, \text{ms}^{-2}$ towards the end of the compaction stage. Sliding was governed according to a Mohr–Coulomb law and during the compaction process, the coefficients of friction for the spheres, sleeper, walls and base were set to be 0.3. During subsequent loading,

Fig. 5 Effect of angle α on clump geometry

$\alpha = 30°$ $\alpha = 40°$ $\alpha = 50°$ $\alpha = 60°$
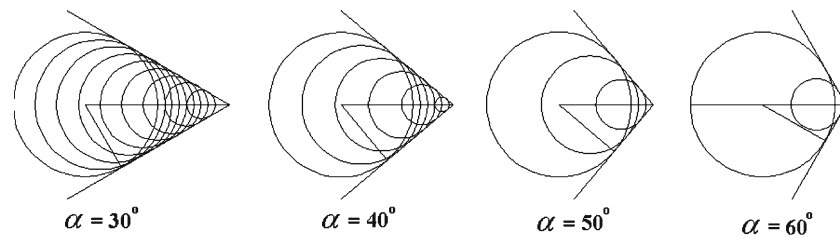
Table 1 Parameters for clumps in Fig. 7

Shape parameters	Samples				
	Sample 1	Sample 2	Sample 3	Sample 4	Sample 5
Number of directions of ball generation	6	14	14	14	6
Probability of the number of directions of ball generation used, p (%)	50	50	50	40	80
Maximum number of balls in each direction	2	2	2	2	2
Maximum reduction of radius in each direction, c	$0.2R$	$0.5R$	$0.2R$	$0.4R$	$0.5R$
D_3	$0.2R$	$0.2R$	$0.2R$	$0.2R$	$0.5R$
Number of balls used in each edge	1	2	2	2	2

Table 2 Parmeters for aggregates of clumps in Figs. 9 and 10

| Shape parameters	Samples	
	Sample 1	Sample 2
Number of directions of ball generation	6	14
Probability of the number of directions of ball generation used, p (%)	50	50
Maximum number of balls in each direction	2	2
Maximum reduction of radius in each direction, c	$0.2R$	$0.5R$
D_3	$0.2R$	$0.2R$
Number of balls used in each edge	1	2

Fig. 6 Formation of edge of clump

the friction coefficients were set equal to 0.5. The normal and shear stiffnesses (linear-elastic) of the spheres were set to be 5.08×10^9 N/m using the procedure documented in the PFC^{3D} Manuals [2] and the stiffnesses of the sleeper and walls were set to have the same values. The stiffnesses of the simulated rubber base were set to 2.54×10^6 N/m following Lim and McDowell [8], and the density of the spheres was 2,600 kg/m^3.

For the clumps, the stiffnesses and coefficients of friction used were the same as for the simulated box tests on spheres; in future work the effect of the local clump radius on the contact stiffness will be studied. During compaction the coefficient of friction of the balls was set to 0.3, and increased to 0.5 after compaction. Frictionless balls were not used during compaction because it was found that it took the clumps a long time to stabilise after compaction, even with the default local non-viscous damping active (PFC^{3D} uses a damping constant applied to the force acting on each particle in order to dissipate energy [2]). The clumps were formed by creating small initial spheres, expanding to a diameter of 36.25 mm and cycling to equilibrium. Virtual spheres

were then created by expanding the spheres by factor of 1.26 for Sample 1 and 1.31 for Sample 2. Each virtual sphere formed the outermost possible boundary for each clump. Figure 9b shows Sample 1, containing 1,770 clumps (17,642 balls) and Fig. 9c shows Sample 2 with 1,995 clumps (65,591 balls). Figure 10 shows the contact forces for each of the three samples under self-weight after compaction by enhanced gravity and then reducing gravity to $9.81\,\text{ms}^{-2}$. It can be seen that the contact forces are reduced and are more homogeneous for the more angular clumps in Fig. 9c, which is in agreement with data published by Nakata et al. [11] for real sands.

It should be noted that for the clumps, since balls overlap, the total volume of balls in a clump is greater than the volume of the clump and the mass of the clump is therefore greater than the mass of an equivalent clump with a uniform density; such an entity is currently not available within PFC^{3D}. Where there is overlapping of balls within a clump, there is a contribution to the mass in the overlapping region from each of the overlapping balls. This also affects the moment of inertia of the clump since the mass is not uniformly distributed within the clump. Thus, a modified density was used in each clump. In order to achieve the desired mass, the
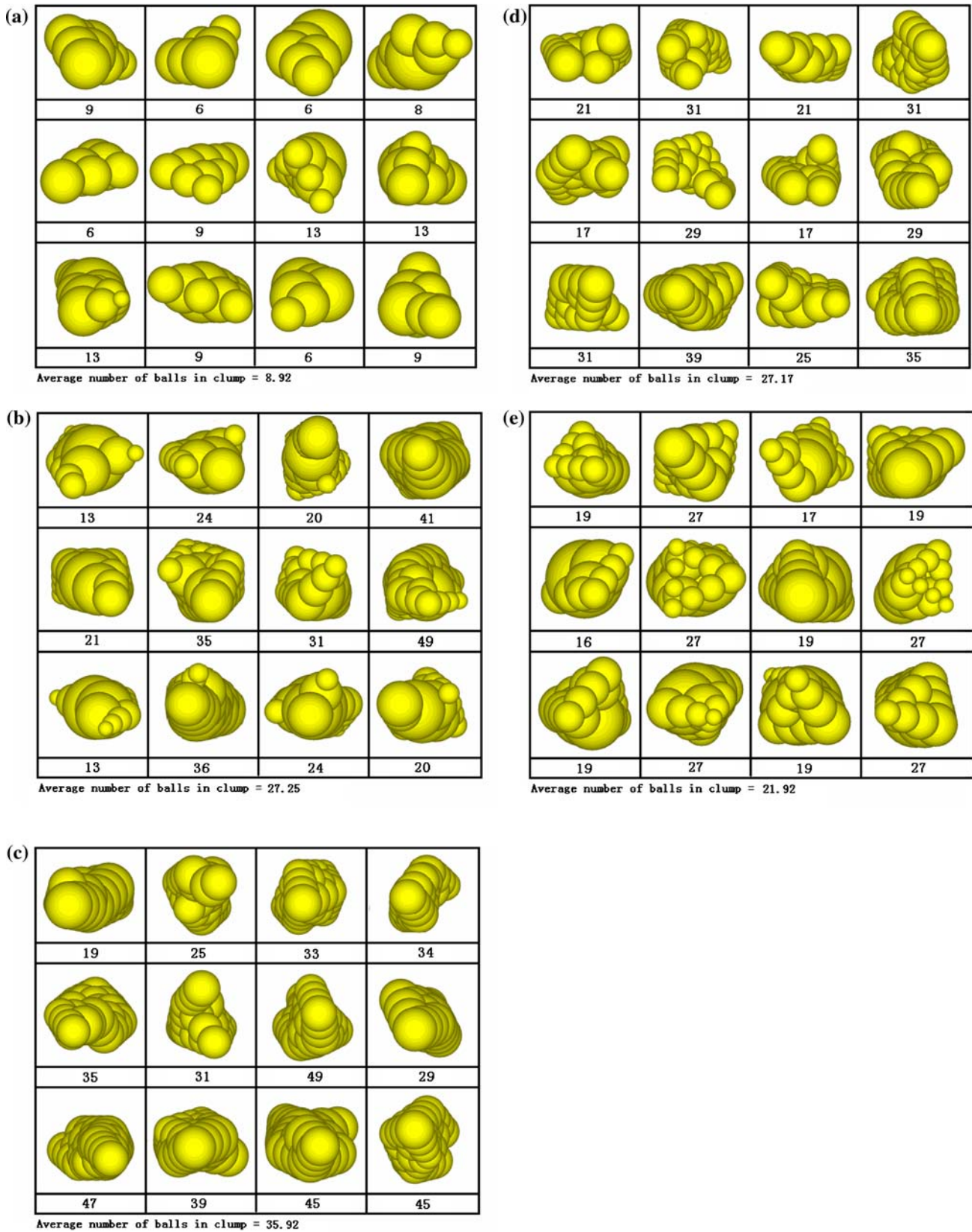
Fig. 7 Typical clumps generated for **a** Sample 1; **b** Sample 2; **c** Sample 3; **d** Sample 4; **e** Sample 5 (refer to Table 1 for parameters)
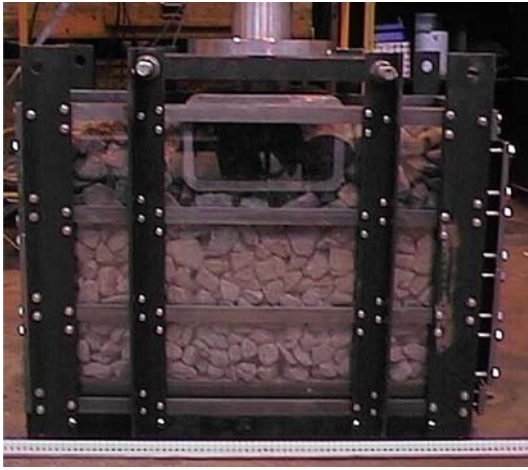
modified density ρ_{m} is derived from the initial density ρ_0 as

$$\rho_{\mathrm{m}} = \frac{V_{\mathrm{clump}} \cdot \rho_0}{\sum V_i} \tag{10}$$

where V_i is the volume of the ith ball in the clump and V_{clump} is the volume of the clump and

$$\sum V_i = \sum V_i^{\mathrm{overlap}} + V_{\mathrm{clump}} \tag{11}$$

where $\sum V_i^{\mathrm{overlap}}$ is the volume of overlap in the clump. This procedure produces clumps with the correct mass but with a non-uniform density. Due to the difficulty in calculating the volume of each clump, and since the geometry of each clump is different, the volume of a clump in (10) was approximated to be equivalent to the volume of a sphere of diameter 36.25 mm (i.e. the volume of the sphere created before expanding to create a virtual sphere to contain the clump). Work is now underway to produce clumps of uniform density. The use of clumps having non-uniform density because of overlapping mass means that the dynamics of the clumps are only approximately correct. The total mass of the clump m, location of the centre of mass of clump $x_i^{[G]}$, and the moments and products of inertia I_{ii} and I_{ij}, are defined by the following equations [2]:

$$m = \sum_{p=1}^{N_p} m^{[p]} \tag{12}$$

$$x_i^{[G]} = \frac{1}{m} \sum_{p=1}^{N_p} m^{[p]} x_i^{[p]} \tag{13}$$

$$I_{ii} = \sum_{p=1}^{N_p} \left\{ m^{[p]} \left(x_j^{[p]} - x_j^{[G]} \right) \left(x_j^{[p]} - x_j^{[G]} \right) \right. \tag{14}$$
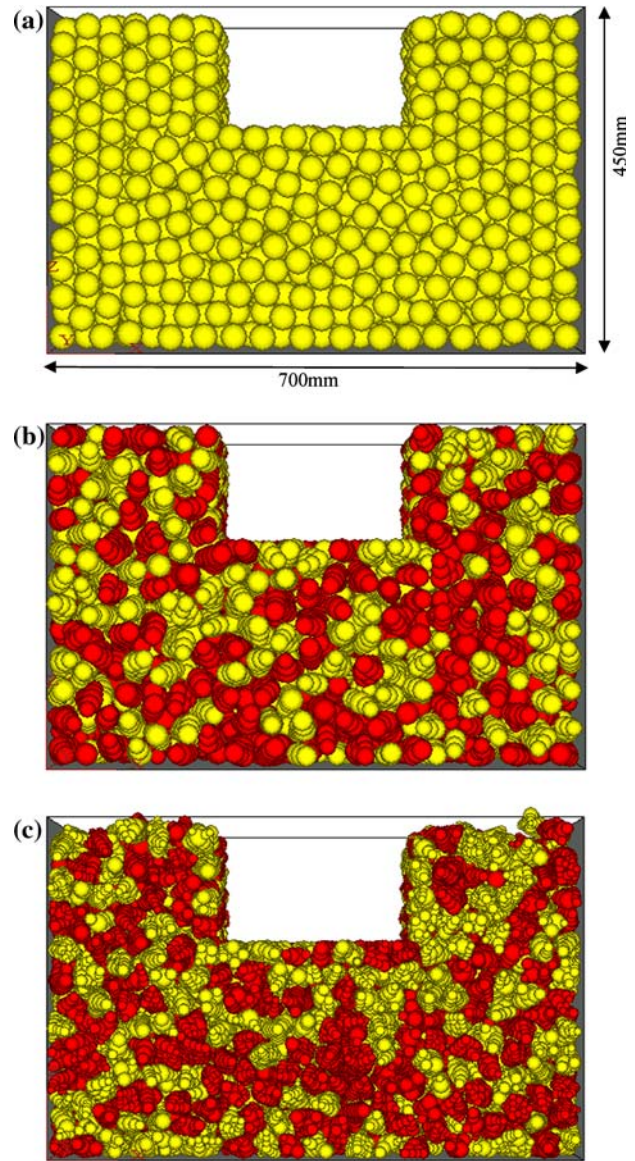
Fig. 9 Box test on **a** spheres, **b** Sample 1 and **c** Sample 2 (Table 2)

$$\left. + \frac{2}{5} m^{[p]} R^{[p]} R^{[p]} \right\}$$

$$I_{ij} = \sum_{p=1}^{N_p} \left\{ m^{[p]} \left(x_i^{[p]} - x_i^{[G]} \right) \left(x_j^{[p]} - x_j^{[G]} \right) \right\} \quad (j \neq i) \tag{15}$$

in which N_p is the number of balls in the clump, $m^{[p]}$ is the mass of a ball, $x^{[p]}$ is the location of the ball and $R^{[p]}$ is the radius of the ball. Since the balls of the clump produced following the simple procedure described in section 2 locate around the first generated sphere, with smaller degrees of overlap occurring further from that sphere, the location of the centre of mass of the clump is very close to the centre of mass of a clump with the
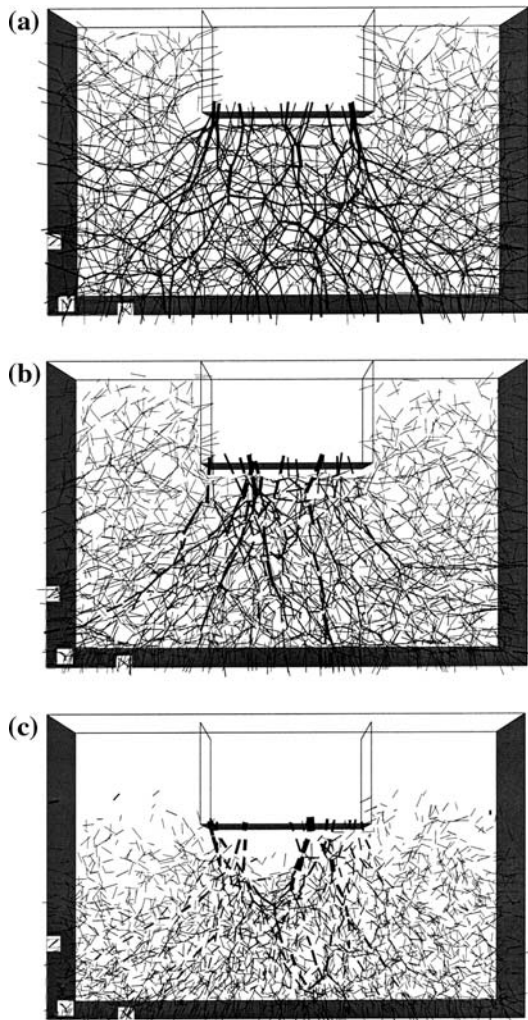
Fig. 10 Contact forces for **a** spheres, **b** Sample 1 and **c** Sample 2 prior to loading

same mass and uniform density. The clump is treated as a rigid body, so its motion is described by the translational motion of the centre of mass in terms of position x_i, velocity $\dot{x}_i$ and acceleration $\ddot{x}_i$ and the rotational motion in terms of the angular velocity ω_i and acceleration $\dot{\omega}_i$. The equation for translational motion is

$$F_i = m(\ddot{x}_i - g_i) \tag{16}$$

where F_i is the resultant force (i.e. the vector sum of the externally applied forces) acting on the clump and g_i is the gravitational body force acceleration vector. The equation for rotational motion is

$$[\mathbf{M}] - [\mathbf{W}] = [\mathbf{I}][\boldsymbol{\alpha}]$$

where

$$[\mathbf{M}] = \begin{bmatrix} \mathbf{M}_1 \\ \mathbf{M}_2 \\ \mathbf{M}_3 \end{bmatrix}$$

$$[\mathbf{W}] = \begin{bmatrix} \omega_2\omega_3(I_{33} - I_{22}) + \omega_3\omega_3 I_{23} - \omega_2\omega_2 I_{32} - \omega_1\omega_2 I_{31} + \omega_1\omega_3 I_{21} \\ \omega_3\omega_1(I_{11} - I_{33}) + \omega_1\omega_1 I_{31} - \omega_3\omega_3 I_{13} - \omega_2\omega_3 I_{12} + \omega_2\omega_1 I_{32} \\ \omega_1\omega_2(I_{22} - I_{11}) + \omega_2\omega_2 I_{12} - \omega_1\omega_1 I_{21} - \omega_3\omega_1 I_{23} + \omega_3\omega_2 I_{13} \end{bmatrix}$$

$$[\mathbf{I}] = \begin{bmatrix} I_{11} & -I_{12} & -I_{13} \\ -I_{21} & I_{22} & -I_{23} \\ -I_{31} & -I_{32} & I_{33} \end{bmatrix}$$

$$[\boldsymbol{\alpha}] = \begin{bmatrix} \alpha_1 \\ \alpha_2 \\ \alpha_3 \end{bmatrix} = \begin{bmatrix} \dot{\omega}_1 \\ \dot{\omega}_2 \\ \dot{\omega}_3 \end{bmatrix} \tag{17}$$

and M_i is the resultant moment about the centre of mass of the clump. Both equations (16) and (17) are solved using a centered finite difference procedure with a time-step of Δt. The quantities $\dot{x}_i$ and ω_i are calculated at the mid-intervals of $t \pm n\Delta t/2$, and the quantities $x_i, \ddot{x}_i, \dot{\omega}_i$, F_i and M_i are computed at the primary intervals of $t \pm n\Delta t$. The solution of (17) requires an iterative procedure, but computational speed is increased by ignoring the non-linear terms and ignoring coupling between angular accelerations. This is achieved by setting both [**W**] and the off-diagonal terms in the inertia tensor [**I**] to zero. This procedure is considered appropriate for quasi-static problems and even for steady flow calculations. The approximation should only result in large errors for large angular velocities. For the simulations presented in this paper, the angular velocities of the clumps are small; so this approximate solution method is appropriate.

For the sample of spheres, it was possible to calculate the porosity directly using a measurement sphere in PFC^{3D}; in this way the variation in the porosity throughout the box can be studied. However, no facility is available in PFC^{3D} for calculating the porosity of a sample of clumps comprising more than two particles within each clump. Therefore the initial porosities of the samples were estimated using a 3-D grid of small cubes, each of side 0.005 m, in the column directly below the sleeper and found to be 0.37 for the aggregate of spheres, 0.35 for Sample 1 and 0.37 for Sample 2. By examining the percentage error in calculating the volume of a sphere, and a two-ball clump and a three-ball clump using this method, it is estimated that the percentage errors in the porosities should be less than 1% for the samples of clumps and should be about 5% for the spheres. This is deemed acceptable, given the variability of porosity within the box.
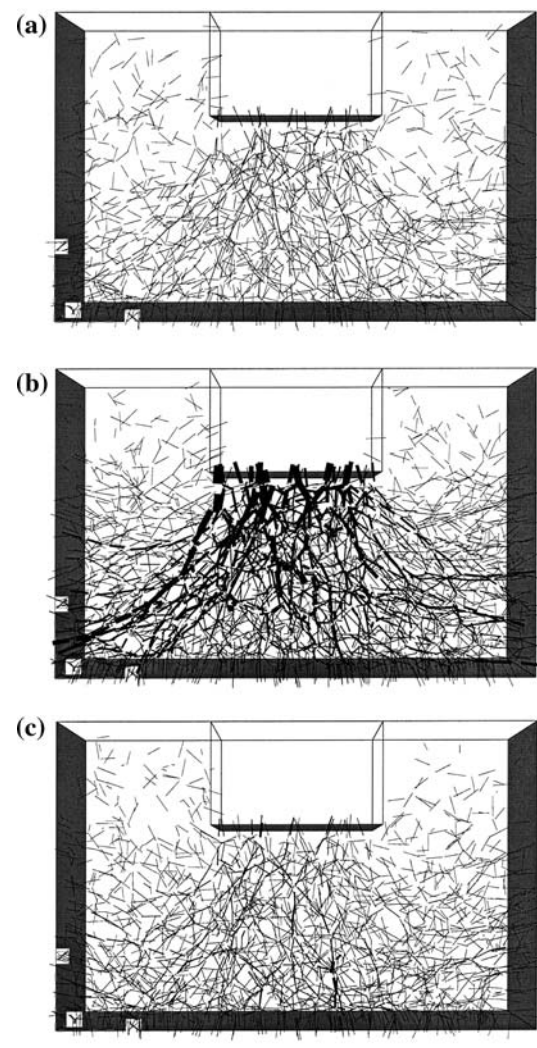
The spheres and Sample 1 were loaded using a sinusoidal load pulse with a minimum load of 3 kN and a maximum load of 40 kN, at a frequency of 3 Hz (following [10]). Figures 11 and 12 show the contact forces for
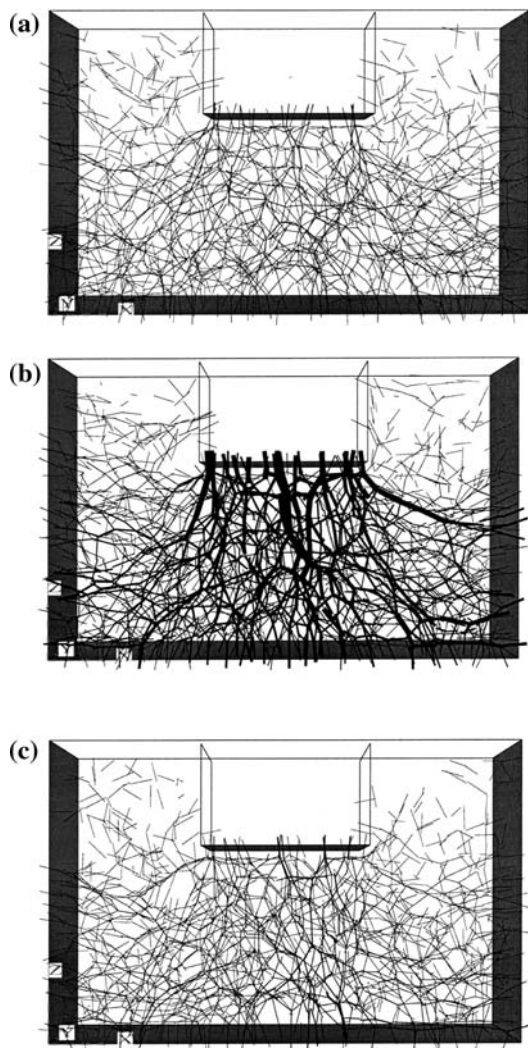
Fig. 11 Contact forces for spheres **a** prior to loading (maximum contact force = 482 N, average contact force = 29.9 N, number of contacts = 10,337); **b** at maximum load (maximum contact force = 4,050 N, average contact force = 336.2 N, number of contacts = 10,323) and **c** after unloading to 3 kN (maximum contact force = 1,012 N, average contact force = 42.7 N, number of contacts = 10,328)

Fig. 12 Contact forces for Sample 1 **a** prior to loading (maximum contact force = 374 N, average contact force = 15.4 N, number of contacts = 282,955); **b** at maximum load (maximum contact force = 4,233 N, average contact force = 164.1 N, number of contacts = 282,955) and **c** after unloading to 3 kN (maximum contact force = 1,354 N, average contact force = 34.4 N, number of contacts = 282,955)

the spheres and Sample 1 prior to loading, at maximum load and after unloading to 3 kN, respectively. It is noted that the number of contacts does not change much during the cycle of loading and unloading. The magnitude of the average of the contact force for the clumps in Sample 1 (which is closer to reality) is less than that for the spheres because the higher number of contacts for Sample 1 leads to a more homogeneous stress distribution.
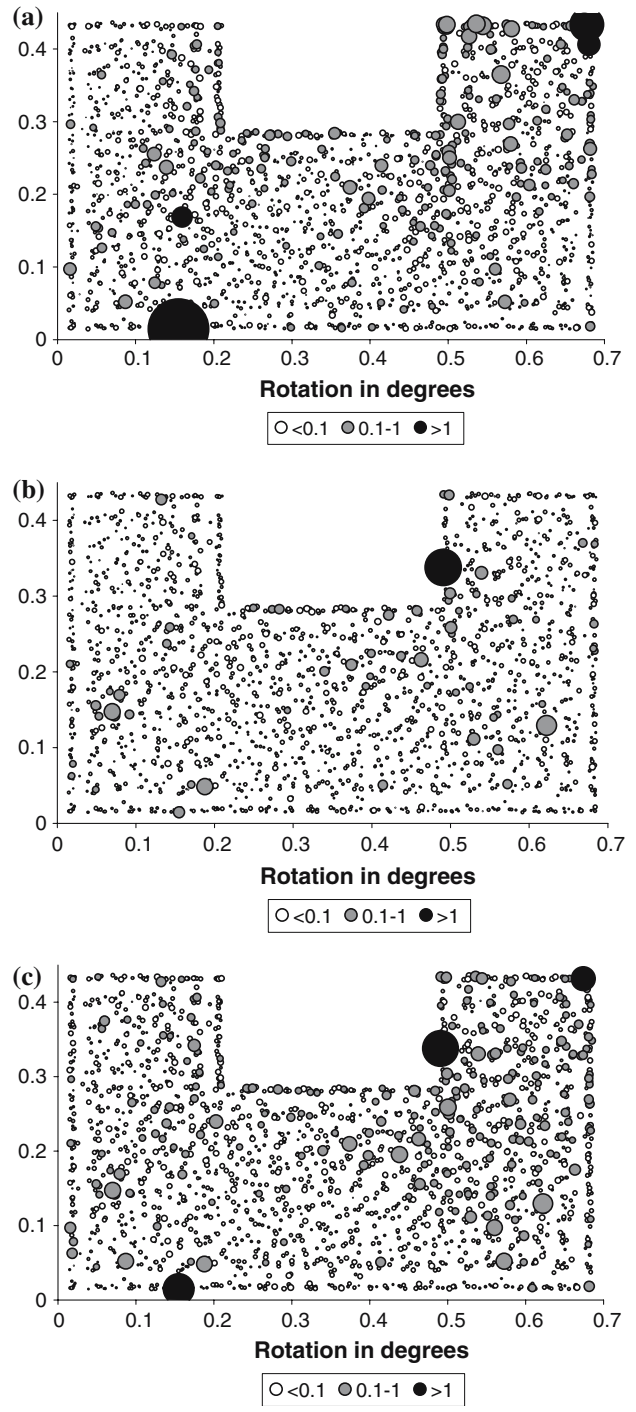
Figures 13 and 14 show the rotations of the spheres and clumps during one cycle of loading. The size of each circle is proportional to the magnitude of the particle rotation, calculated as the vector sum of the rotations

about three mutually orthogonal axes. The grey circles reflect a rotation of 10°–20° for the spheres and 0.1°–1° for the clumps in Sample 1. Solid black circles indicate larger rotations of >20° for spheres and >1° for clumps. For the sample of spheres, it is clear that the main particle rotations occur near the corner of the sleeper and both sides of the sleeper. Less rotation occurs directly below the sleeper. In Sample 1, the distribution of the rotations is quite uniform except for a few particles which have relatively large rotations, and the average particle rotation is much less than for the spheres. The magnitude of the average rotation of the spheres after the complete cycle of loading and unloading is almost
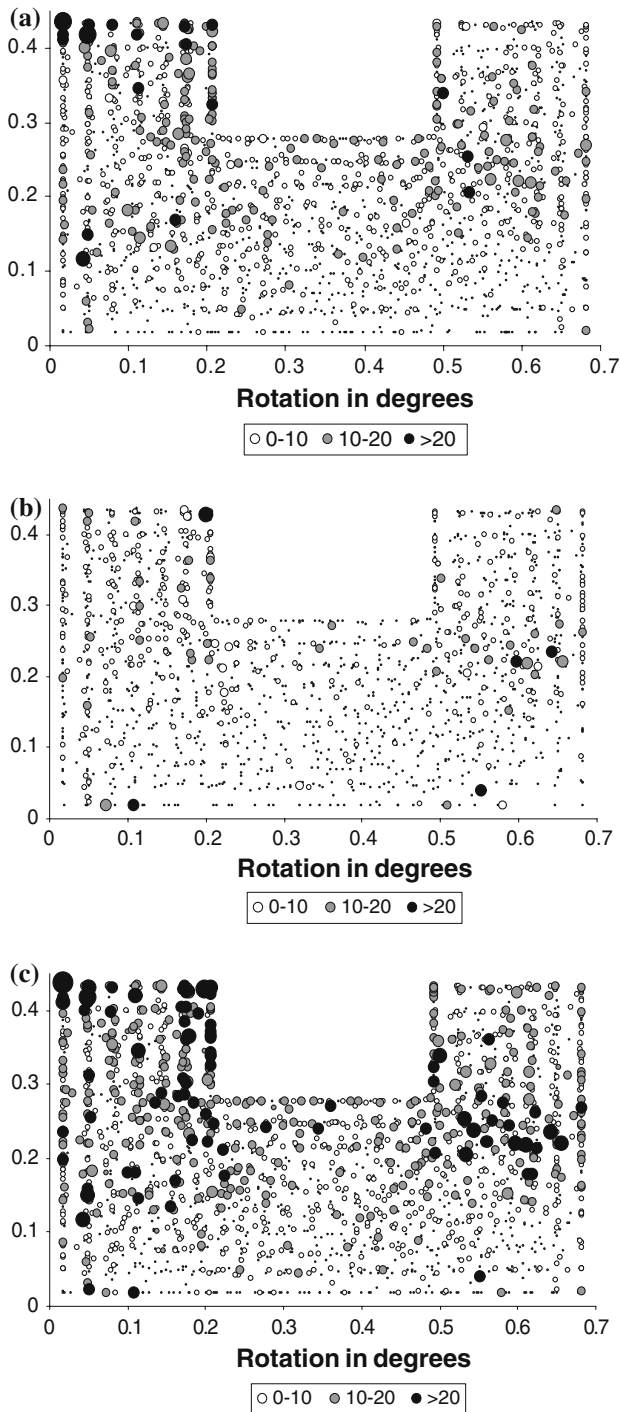
Fig. 13 Rotations of spheres **a** during loading (maximum rotation = 48.3°, average rotation = 5.18°; **b** during unloading (maximum rotation = 26.5°, average rotation = 2.92°) and **c** after the complete cycle of loading and unloading (maximum rotation = 63.2°, average rotation = 7.25°)

Fig. 14 Rotations of clumps in Sample 1 **a** during loading (maximum rotation = 8.89°, average rotation = 0.061°); **b** during unloading (maximum rotation = 3.15°, average rotation = 0.033°) and **c** after the complete cycle of loading and unloading (maximum rotation = 3.31°, average rotation = 0.062°)

equal to the summation of the magnitudes of the average rotation during loading and during unloading separately. Similarly, the magnitude of the maximum rotation after the load–unload cycle is much greater than that at maxi-
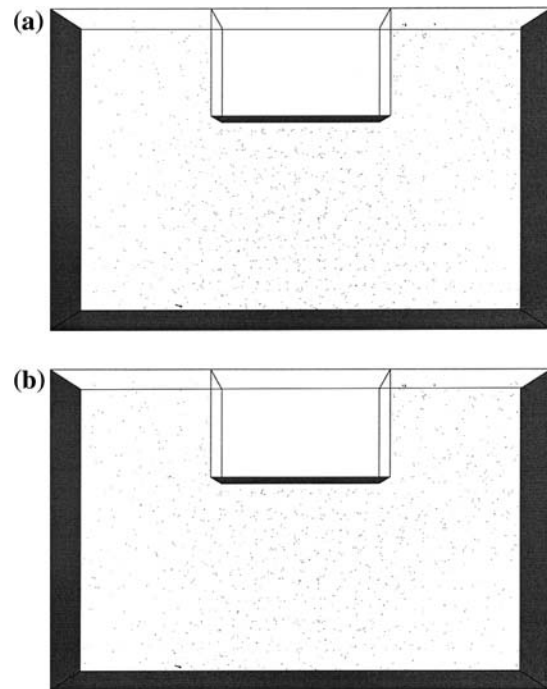
mum load. This shows that spheres continue to roll in the same sense even on unloading. However, in Sample 1 the magnitude of the average particle rotation of the clumps after the complete cycle of loading and unloading is sim-
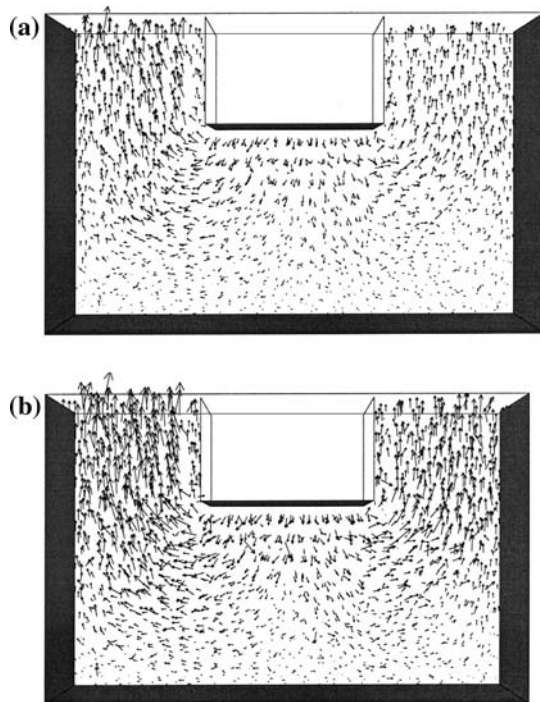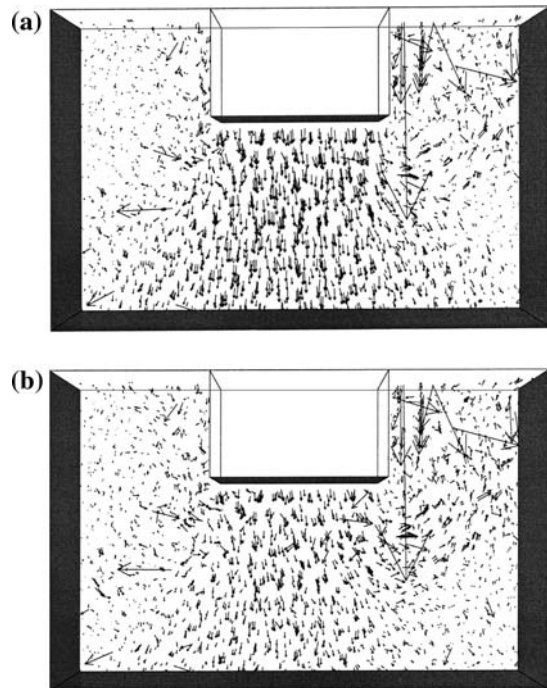
Fig. 15 Total displacements of spheres **a** at maximum load (maximum displacement = 8.25 mm); and **b** after one cycle of loading and unloading (maximum displacement = 11.79 mm)


Fig. 16 Total displacements for clumps in Sample 1 **a** at maximum load (maximum displacement = 2.34 mm) and **b** after one cycle of loading and unloading (maximum displacement = 2.32 mm)

ilar to that at maximum load, and it can be seen that the maximum rotation after the load–unload cycle is much less than that maximum load. This indicates that for the clumps, some particles must have rolled in the opposite sense by a significant amount on unloading. Thus the influence of three-dimensional particle shape can be seen in providing interlock and thus reduced particle rotation. The multiple contacts between clumps give increased rolling resistance.

Figures 15 and 16 show the particle displacement vectors for the spheres and Sample 1 drawn at the same scale. Since the particle displacements for Sample 1 are so small, this scale has been magnified by a factor of 80 and reproduced in Fig. 17a and b. It can be noted that the displacements of the spheres on both sides of the sleeper are larger than those below the sleeper and the displacements are generally upwards. Comparing Fig. 15a and b, it can be noted that the spheres on both sides of the sleeper continue to move upwards on unloading. For the clumps, the behaviour is very different: the average particle displacement is greatest directly beneath the sleeper and is downwards. Comparing Fig. 17a and b, it can be seen that the clumps below the sleeper must have moved upwards during unloading. The displacements of Sample 1 seem closer to the response of ballast particles in the box test [10].

Fig. 17 Displacement vectors of **a** Fig. 16a and **b** Fig. 16b magnified by a factor of 80

Figure 18 shows the response of the spheres (Test A) and Sample 1 in Fig. 9, Table 2 (Test B) to a single cycle of load (sinusoidal, at frequency 3 Hz and maximum load

Fig. 18 Cyclic response for spheres (Test A) and Sample 1 (Test B)
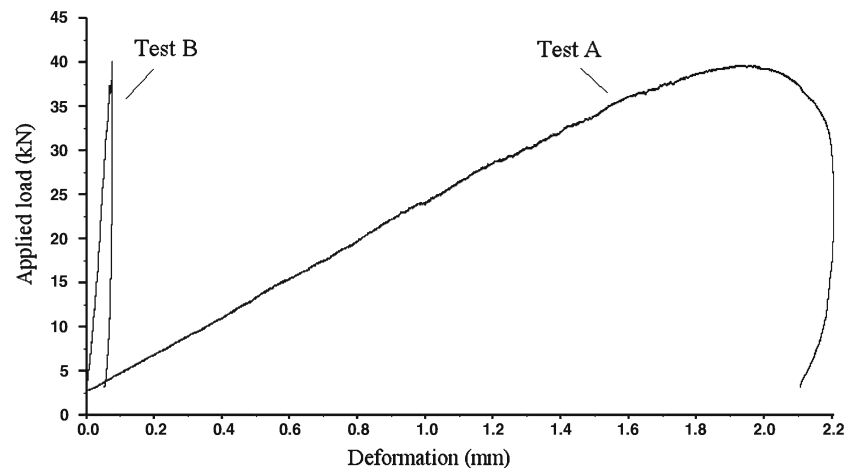
of 40 kN). It can be seen that the clumps show a more realistic load-deformation response than the spheres, comparing with available data for the cyclic loading of granular materials [12], in which it is usually observed that axial strain does not continue to increase beyond maximum load, but rather reduces in a resilient manner on unloading. The difference in the response of the spheres and Sample 1 can be attributed to the interlocking provided by the three-dimensional clumps, which affects the rolling resistance and particle displacements, as shown in Figs. 13, 14, 15, 16 and 17. This is consistent with 3D simulations using PFC by Suiker and Fleck [13] in which they showed that restricting particle rotation may substantially increase the overall frictional resistance of the spheres. The use of clumps generated using the simple procedure described above therefore looks to be a promising tool for generating more realistic ballast particle shapes and consequently a more realistic load-deformation response.

4 Conclusions

The discrete element method has been used to simulate particles of railway ballast. A simple procedure has been developed which permits the generation of clumps of spheres to simulate ballast in a realistic way. Simple parameters have been shown to allow control over the sphericity, angularity and surface roughness, and examples of various clumps generated at random using the procedure have been described. Aggregates of clumps have been generated in a box and the stresses induced by self-weight are found to become more homogeneous with increasing angularity of the clump, in agreement with available data. The interlocking provided by the three-dimensional clumps gives much reduced particle rotations and displacements. For the spheres, deforma-

tion is concentrated at the corners and sides of the sleeper where particles flow upwards, even on unloading. For the clumps, however, deformation is concentrated directly under the sleeper where particles move downwards on loading, and then upwards by a smaller amount on unloading, giving a hysteretic load-deformation response of the clumps which is found to resemble more closely the response of real ballast. Because the mass of a clump is the sum of the individual masses of the constituent balls, the density has been scaled to achieve clumps of the correct mass. However, such clumps will have non-uniform density. Future work will adopt the described procedure for the generation of clumps of a desired shape, but with uniform density within the clump, in addition to studying the response of an assembly of clumps subjected to many cycles of load.

References

1. Cundall, P.A., Strack, O.D.L.: A discrete element model for granular assemblies. Géotechnique **29**(1), 47–65 (1979)
2. Itasca, Particle Flow Code in Three Dimensions. Itasca Consulting Group, Inc., Minnesota, 1999
3. McDowell, G.R., Harireche, O.: Discrete element modelling of soil particle fracture. Géotechnique **52**(2), 131–135 (2002)
4. Robertson, D.: Computer simulations of crushable aggregates. Ph.D. dissertation, Cambridge University (2000)
5. McDowell, G.R., Harireche, O.: Discrete element modelling of yielding and normal compression of sand. Géotechnique **52**(4), 299–304 (2002)
6. Cheng, Y.P., Nakata, Y., Bolton, M.D.: Discrete element simulation of crushable soil. Géotechnique **53**(7), 633–641 (2003)
7. Harireche, O., McDowell, G.R.: Discrete element modelling of cyclic loading of crushable aggregates. Granul Matter **5**(3), 147–152 (2003)
8. Lim, W.L., McDowell, G.R.: Discrete element modelling of railway ballast. Granular Matter **7**(1), 19–29 (2005)
9. Railtrack, Railtrack Line Specification RT/CE/006 Issue 3: Track Ballast. Railtrack, London (2000)

10. McDowell, G.R., Lim, W.L., Collop, A.C., Armitage, R., Thom, N.H.: Comparison of ballast index tests for railway trackbeds. In: Proceedings of the Institution of Civil Engineers – Geotechnical Engineering, 157(GE3), p. 151–161 (2004)

11. Nakata,Y., Kato, Y., Hyodo, M., Hyde, A.F.L., Murata, H.: One-dimensional compression behaviour of uniformly graded sand related to single particle crushing strength. Soils and Foundations 41(2), 39–51 (2001)

12. Lekarp, F., Isacsson, U., Dawson, A.R.: State of the art. I. Resilient response of unbound aggregates. ASCE J. Transport Eng **126**(1), 66–75 (2000)

13. Suiker, A.S.J., Fleck, N.A.: Frictional collapse of granular assemblies. J Appl Mech **71**, 350–358 (2004)